Mon. Not. R. Astron. Soc. **000**, 1–15 (2013) Printed 8 January 2014 (MN LATEX style file v2.2)

Multi-wavelength Observations of the Binary System PSR B1259−63/LS 2883 Around the 2010-2011 Periastron Passage

M. Chernyakova[1,2], A. A. Abdo[3], A. Neronov [4], M. V. McSwain[5], J. Moldón[6,7], M. Ribó[6], J.M. Paredes[6], I. Sushch[8,9,10], M. de Naurois[11], U. Schwanke[10], Y. Uchiyama[12,13], K. Wood[14], S. Johnston [15], S. Chaty [16,17], A. Coleiro [16] D. Malyshev[4,18], Iu. Babyk[1,2]

[1] *Dublin City University, Dublin 9, Ireland*
[2] *Dublin Institute for advanced studies, 31 Fitzwilliam Place, Dublin 2, Ireland*
[3] *Operational Evaluation Division, Institute for Defense Analyses, 4850 Mark Center Drive Alexandria, VA 22311-1882*
[4] *INTEGRAL Science Data Center, Chemin d'Écogia 16, 1290 Versoix, Switzerland*
[5] *Department of Physics, Lehigh University, 16 Memorial Drive East, Bethlehem, PA, USA*
[6] *Departament d'Astronomia i Meteorologia, Institut de Ciències del Cosmos, Universitat de Barcelona, IEEC-UB, Martí i Franquès 1, E-08028 Barcelona, Spain*
[7] *The Netherlands Institute for Radio Astronomy (ASTRON), 7990-AA Dwingeloo, The Netherlands*
[8] *Centre for Space Research, North-West University, Potchefstroom Campus, 2520, Potchefstroom, South Africa*
[9] *Astronomical Observatory of Ivan Franko National University of L'viv, vul. Kyryla i Methodia, 8, L'viv 79005, Ukraine*
[10] *Institut für Physik, Humboldt-Universität zu Berlin, Newtonstr. 15, D 12489 Berlin, Germany*
[11] *Laboratoire Leprince-Ringuet, Ecole Polytechnique, CNRS/IN2P3, F-91128 Palaiseau, France*
[12] *SLAC National Accelerator Laborat 2575 Sand Hill Road, Menlo Park, CA 94025, USA*
[13] *Department of Physics, Rikkyo University, Nishi-Ikebukuro 3-34-1, Toshima-ku, Tokyo, JAPAN 171-8501*
[14] *U.S. Naval Research Lab 4555 Overlook Ave., SW Washington, DC 20375, USA*
[15] *CSIRO Astronomy and Space Science, PO BOX 76, NSW 1710, Australia*
[16] *Laboratoire AIM (UMR-E 9005 CEA/DSM - CNRS - Université Paris Diderot), Irfu / Service d'Astrophysique, CEA-Saclay, 91191 Gif-sur-Yvette Cedex, France*
[17] *Institut Universitaire de France, 103 Boulevard Saint Michel, 75006 Paris, France*
[18] *Bogolyubov Institute for Theoretical Physics,14-b Metrolohichna street, Kiev, 03680, Ukraine*

arXiv:1401.1386v1 [astro-ph.HE] 7 Jan 2014

Received <date> ; in original form <date>

ABSTRACT

We report on broad multi-wavelength observations of the 2010-2011 periastron passage of the γ-ray loud binary system PSR B1259−63. High resolution interferometric radio observations establish extended radio emission trailing the position of the pulsar. Observations with the *Fermi Gamma-ray Space Telescope* reveal GeV γ-ray flaring activity of the system, reaching the spin-down luminosity of the pulsar, around 30 days after periastron. There are no clear signatures of variability at radio, X-ray and TeV energies at the time of the GeV flare. Variability around periastron in the Hα emission line, can be interpreted as the gravitational interaction between the pulsar and the circumstellar disk. The equivalent width of the Hα grows from a few days before periastron until a few days later, and decreases again between 18 and 46 days after periastron. In near infrared we observe the similar decrease of the equivalent width of Brγ line between the 40th and 117th day after the periastron. For the idealized disk, the variability of the Hα line represents the variability of the mass and size of the disk. We discuss possible physical relations between the state of the disk and GeV emission under assumption that GeV flare is directly related to the decrease of the disk size.

Key words: gamma rays: stars – pulsars: individual: PSR B1259−63 – stars: emission-line, Be – X-rays: binaries – X-rays: individual: PSR B1259−63

1 INTRODUCTION

The binary system PSR B1259−63 is comprised of a 47.76 ms radio pulsar in a highly eccentric orbit ($e \approx 0.87, P \approx 3.4$ years) around the massive main sequence O9.5Ve star LS 2883 (Johnston et al. 1992; Negueruela et al. 2011). The companion shows evidence for an equatorial disk in its optical spectrum, and it has generally been classified as a Be star. The minimum approach between the pulsar and massive star is about $\sim$ 0.9 astronomical unit (AU) (Negueruela et al. 2011), which is roughly the size of the equatorial disk (Johnston et al. 1992). The orbital plane of the pulsar is thought to be inclined with respect to this disk, so it crosses the disk plane twice each orbit, just before and just after the periastron passage (e.g. Melatos, Johnston & Melrose 1995). A shock interaction between the relativistic pulsar wind and the wind and photon field

© 2013 RAS

of the Be star is believed to give rise to the observed unpulsed X-ray emission observed throughout the orbit (Hirayama et al. 1999; Chernyakova et al. 2006) and the unpulsed radio and TeV γ-rays observed within a few months of periastron passage (Johnston et al. 1999, 2005; Kirk, Ball & Skjaeraasen 1999; Aharonian et al. 2005, 2009).

The emission from the system varies dramatically as the pulsar moves through very different environments, making it an excellent test bed for models of a shocked pulsar wind. When the pulsar is far from periastron, the highly linearly polarized pulsed radio emission is detected (Johnston et al. 1999, 2005). As the pulsar approaches the companion star ($\sim t_{\rm p} - 100$ days, where $t_{\rm p}$ is the time of periastron passage), depolarization of the pulsed emission occurs, and the dispersion measure (DM) and absolute value of the rotation measure (RM) begin to increase while the pulsed flux density decreases (Johnston et al. 1996). In the range $\sim t_{\rm p} \pm 15$ days, no pulsed flux is detected (Johnston et al. 1996). The eclipse of the pulsar during this period is likely due to absorption and severe pulse scattering by the Be star's disk (Johnston et al. 1996). This eclipse of the pulsed emission is accompanied by an increase in the unpulsed radio flux beginning at $\sim t_{\rm p} - 30$ days and reaching a maximum at about $t_{\rm p} - 10$ days. It then decreases around the periastron passage before climbing to a second peak about 20 days after the periastron passage (Johnston et al. 1999, 2005), finally declining over $\sim t_{\rm p} + 100$ days. Unpulsed flux at the two peaks before and after periastron passage can be several times higher than the value during the periastron passage.

The radio emission has been imaged at scales of AU with the Australian Long Baseline Array, revealing that it extends up to projected distances of more than 100 AU close to the periastron passage (Moldón et al. 2011). The peak of this radio emission is detected at projected distances of several tens of AU outside the binary system (provided unmodeled ionospheric uncertainties are not very large). This has been the first observational evidence that non-accreting pulsars orbiting massive stars can produce variable extended radio emission at AU scales. It must be noted that similar structures have been detected in the γ-ray binaries LS 5039 and LS I +61 303, reinforcing the links between these three sources and supporting the presence of pulsars in these systems as well (Moldón, Ribó & Paredes 2012 and references therein).

In the X-ray band, variable unpulsed emission is observed throughout the orbit (Chernyakova et al. 2009 and references therein), even at apastron. For most of the orbit, the typical X-ray flux is on the order of $F_{\rm X} \sim 10^{-12}$ erg cm^{-2} s^{-1}. Commencing 20–30 days prior to periastron passage, there is a sharp rise, reaching 10–20 times the apastron flux. After that, the flux decreases by a factor of a few to a local minimum near or after periastron passage, then to a post-periastron second maximum similar to the pre-periastron maximum, following which it declines over 100–150 days. This twofold X-ray maximum broadly resembles the unpulsed radio light curve. Moreover, the X-ray pattern is essentially repeated during each orbit, without large orbit-to-orbit variations.

Apart from the variable X-ray emission from the binary system itself, Pavlov, Chang & Kargaltsev (2011) have recently reported the discovery of extended X-ray emission on distance scales much larger than the size of the binary orbit (4″, corresponding to a projected distance of $\sim 10^{17}$ cm). This indicates that the pulsar is also powering a "regular" pulsar wind nebula during the periods outside the periastron passage.

At energies around 1 GeV, the *Energetic Gamma-Ray Experiment Telescope (EGRET)* produced only an upper limit for the 1994 periastron passage ($F_\gamma \leqslant 9.4 \times 10^{-8}$ photons cm^{-2} s^{-1} for $E \geqslant$ 300 MeV, 95% confidence (Tavani et al. 1996)), and there was no opportunity to observe at these energies during the next four periastron passages. However, in TeV γ-rays the system was detected during the 2004 and 2007 periastron passages (Aharonian et al. 2005, 2009), and flux variations on daily timescales from zero to 10^{-11} cm^{-2} s^{-1} were seen for energies >0.38 TeV in 2004 (Aharonian et al. 2005). A combined lightcurve of those two periastron passages reveals a hint of two asymmetrical peaks centered around periastron with a decrease of the flux at the periastron itself. Peaks of the TeV emission roughly coincide with the flux enhancement observed in other wavebands as well as the eclipse of the pulsed radio emission. In 2007, the photon flux became notable at the level of 3 standard deviations (σ) from $\sim t_{\rm p} - 75$ days onwards. No TeV detection has been reported far from periastron (Aharonian et al. 2009).

The most recent periastron passage took place on 2010 December 14, 16:40:50.6 (MJD 55544.7). For the first time, we had a chance to observe it in GeV range with the Large Area Telescope (LAT) of *Fermi* satellite. No detection at the level of 5σ was observed from the source on daily and weekly timescales prior to 28 days before the periastron, $t_{\rm p} - 28$ days. Integrating from $t_{\rm p} - 28$ days (the typical start of enhanced X-ray and unpulsed radio flux) to periastron yielded a clear detection of excess γ-ray flux from the source at a 5σ level in the energy range 0.1–1 GeV. The source disappeared after $t_{\rm p} + 18$ days and suddenly become bright again thirty days after the periastron, reaching a flux ∼10 times higher than the integrated flux measured during the periastron passage, (Tam et al. 2011; Abdo et al. 2011b). This flare lasted for about 7 weeks with no corresponding rise in X-ray or radio domains (Abdo et al. 2011b).

Here we report on the multi-wavelength observations of PSR B1259−63 over ∼ 20 decades of energy, from radio to TeV γ-rays, during its 2010 periastron passage. The paper is organized in the following way: in Sect. 2 we describe radio observations, in Sect. 3 we report NIR observations, in Sect. 4 we discuss optical observations, Sects. 5, 6, and 7 are devoted to X-ray, GeV and TeV observations, respectively. The discussion of all the results is in Sect. 8, and finally the conclusions are in Sect.9.

2 RADIO OBSERVATIONS AND RESULTS

2.1 Pulse Monitoring with Parkes

PSR B1259−63 is one of the pulsars regularly timed with the Parkes radio telescope as part of the *Fermi* timing consortium (Smith et al. 2008; Weltevrede et al. 2010). In order to look for changes in the DM and RM and to determine the duration of the eclipse of the pulsed signal, we monitored the pulsar with Parkes during the 2010 periastron passage. The last detection of pulsed emission in 2010 happened eighteen days before the periastron ($t = t_{\rm p} - 18$ days). The first observation with no pulsations happened at $t_{\rm p} - 16$ days. Significant changes in the DM were observed during ∼ 2 weeks leading to the disappearance of the pulse. Pulsation was re-detected on $t_{\rm p} + 15$ days at 3.1 GHz and subsequently at lower frequencies ($t_{\rm p} + 16$ days at 1.4 GHz). The moments when the pulsed emission disappears (last detection) and reappears (first detection) are marked with dashed lines in Fig. 1.

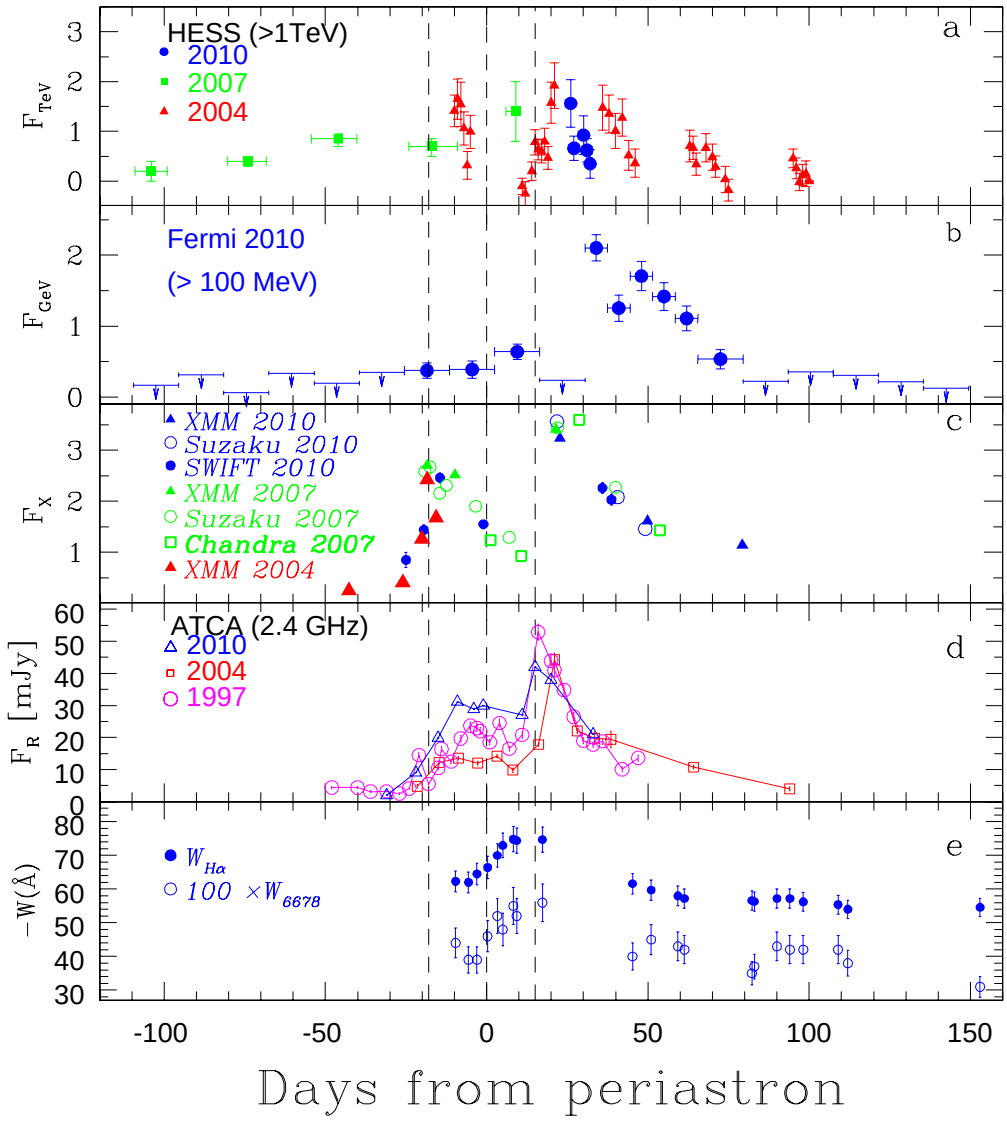

Figure 1. Orbital light curves of PSR B1259−63 around periastron for several passages. *Panel a*: observations by H.E.S.S. in the $E > 1$ TeV energy range for the 2004, 2007, and 2010 periastron passages (Aharonian et al. 2005, 2009; H.E.S.S. Collaboration et al. 2013). Flux is given in 10^{-12} cm^{-2} s^{-1}. *Panel b*: *Fermi*-Ł flux measurements in the $E > 100$ MeV energy range for the 2010 periastron passage. Flux is given in 10^{-6} cm^{-2} s^{-1}. *Panel c*: X-ray fluxes from three periastron passages (Abdo et al. 2011b; Chernyakova et al. 2009). Flux is given in 10^{-11} erg cm^{-2} s^{-1}. The typical error of the X-ray data is smaller than the size of the symbols. *Panel d*: Radio (2.4 GHz) flux densities measured at ATCA for the 2010, 2004 and 1997 periastron passages (Abdo et al. 2011b; Johnston et al. 2005, 1999). Dashed lines correspond to the periastron and to the moments of disappearence (last detection) and reappearence (first detection) of the pulsed emission. *Panel e*: Evolution of the equivalent widths of Hα (filled circles) and He I λ6678 (open circles). W_{6678} is shown multipled by a factor of 100 for easier comparison to $W_{\rm H\alpha}$.

2.2 ATCA Observations

Monitoring of the unpulsed radio signal was performed with the Australia Telescope Compact Array (ATCA). We monitored PSR B1259−63 at frequencies between 1.1 and 10 GHz. A total of twelve observations were collected in the period between $t_{\rm p}$ − 31days and $t_{\rm p}$ + 55 days. Unpulsed radio emission was detected throughout the periastron passage with a behavior similar to that seen in previous periastron passages (Johnston et al. 2005; Abdo et al. 2011b). Panel (d) of Fig. 1 shows the radio light curve for the 1997, 2004 and 2010 periastron passages.

2.3 LBA observations of PSR B1259−63

2.3.1 LBA Observations and Data Reduction

Very Long Baseline Interferometer (VLBI) observations of PSR B1259−63 were conducted with the Australian Long Baseline Array (LBA) at 2.3 GHz (13 cm) on 2011 January 13 (MJD 55574), from 12:00 to 23:55 UTC. The orbital phase of the binary system during the observation was 0.243, computed using the ephemerides in Wang, Johnston & Manchester (2004), and corresponds to 29.3 days after the periastron passage. Six antennas participated in the observations: ATCA (as a phased array), Ceduna,

Hobart, Mopra, Parkes, and Tidbinbilla (we note that the data from Tidbinbilla could not be properly calibrated and were not included in the final data reduction).

The data were obtained with dual circular polarization. ATCA, Mopra, and Parkes recorded eight 16 MHz subbands (four for each right- and left-handed polarization) for a total data bit-rate of 512 Mbps per station, and the rest of the antennas recorded four 16 MHz subbands, for a total bit-rate of 256 Mbps. The correlation of the data was conducted at the correlator in the International Centre for Radio Astronomy Research (ICRAR), which produced the final visibilities with an integration time of 2 seconds. Two passes of the correlator were conducted: one with all the data and for all sources, and a second one correlated only during the on-pulse of PSR B1259−63 using pulsar binning. The pulsar ephemerides were obtained from long-term timing observations conducted with Parkes.

The observations were performed using phase referencing on the calibrator J1256−6449, located at 1.2° from PSR B1259−63. J1256−6449 was correlated at $\alpha_{J2000.0} = 12^h56^m03\overset{s}{.}4032$ and $\delta_{J2000.0} = -64°49'14\overset{''}{.}814$, which has an absolute uncertainty in the ICRF (International Celestial Reference Frame) of 2.8 mas in right ascension and in declination. The cycle time was 6 minutes, spending half of the time on the phase calibrator and the target source alternatively. The sources J1332−6646 and J1352−4412 were observed as fringe finders.

The data reduction was performed using the NRAO Astronomical Image Processing System (AIPS)[1]. We applied a priori flagging on telescope off-source times because of antenna slewing, and ionospheric corrections obtained from total electron content (TEC) models based on GPS data obtained from the Crustal Dynamics Data Information System (CDDIS) data archive[2]. The amplitude calibration was performed using the system temperatures measured at each station, although no antenna gain curves were available. The amplitude calibration was fixed by scaling the individual antenna gains by a factor obtained from the phase calibrator and fringe-finder models. This correction scales the visibility amplitudes between antennas, and therefore the measured source flux density is not reliable. The phase calibration was obtained from the phase reference calibrator J1256−6449 using the AIPS task FRING. The phase solutions were applied to the data of PSR B1259−63. We produced an image of PSR B1259−63 using the task IMAGR, with robust parameter 0, and *uv* tapering of 8 Mλ to reduce the weight of the longest and more noisy baselines. We further calibrated the data with several iteration steps of phase only and phase+amplitude self-calibrations. Due to the limited number of antennas, for amplitude self-calibration we always used integration time intervals of at least 6 hours (half of the total 12-hour observation time). The integration time of the phase self-calibration steps was 10 minutes, and this was reduced to 2 and 1 minutes in the last steps.

The amplitude and phase calibration tables from the phase reference source were also applied to the on-pulse data of PSR B1259−63. In this data set the flux density of the pulsed emission is slightly enhanced, whereas for the unpulsed emission, i.e. extended nebula, it remains equal. We produced self-calibrated images following the same procedure described above. We subtracted the image obtained using the whole data from the image obtained using the on-pulse data only, taking into account a scaling factor for the amplitudes. The resulting image shows a point-like source at the position of the enhanced pulsed emission and therefore marks the position of the pulsar.

[1] AIPS is available online at http://www.aips.nrao.edu/
[2] CDDIS is available online at http://cddis.nasa.gov/

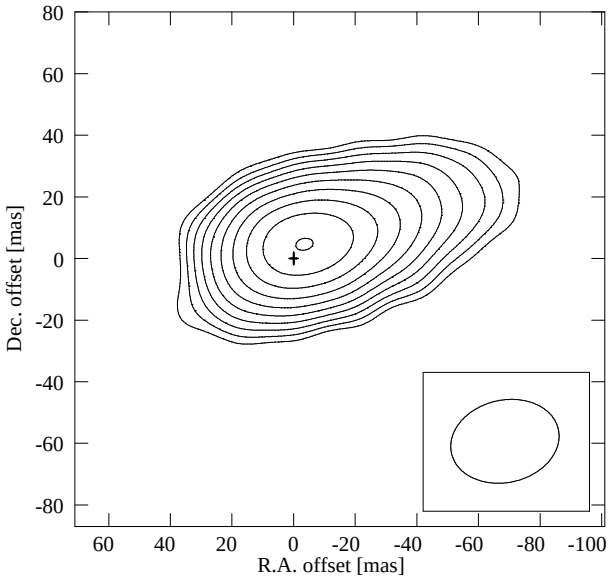

Figure 2. Self-calibrated LBA image of PSR B1259−63 obtained on 2011 January 13 (29 days after periastron passage) at 2.3 GHz frequency. The contours start at 3 times the rms of the image and increase by factors of $2^{1/2}$, up to a peak signal-to-noise ratio of 68. The (0,0) coordinates correspond to the position of the pulsar. The cross represents the pulsar position uncertainty at the 5-σ level. The synthesized beam, plotted in the lower right corner, has a size of 35.5×26.7 mas^2 and is oriented with P.A. of $-77.1°$.

2.3.2 LBA Results

The phase-referenced data provide an accurate determination of the position of PSR B1259−63 with respect to the phase calibrator. The measured position of the peak of the source in the ICRF is $\alpha_{J2000.0} = 13^h02^m47\overset{s}{.}64239 \pm 0.3$ mas (±2.8 mas), and $\delta_{J2000.0} = -63°50'08\overset{''}{.}6267 \pm 0.3$ mas (±2.8 mas), where the first set of uncertainties correspond to the formal errors of a Gaussian fit obtained with JMFIT within AIPS, and the uncertainties in parenthesis correspond to the absolute uncertainty of the phase calibrator position in the ICRF. Additional systematic errors due to the unmodeled ionosphere of 1–5 mas are expected. We note that the source is intrinsically extended (see Moldón et al. 2011) and therefore the astrometry depends on the resolution of the observation, which for the phase-referenced image is 18.4×14.6 mas^2 at 87°.

In Fig. 2 we show the final self-calibrated image of PSR B1259−63 obtained 29 days after the periastron passage. The structure is similar to the one reported in Moldón et al. (2011) 21 days after the previous periastron passage. The source shows a main core and extended diffuse emission towards the North-West. In this image, for the first time, we have an accurate position of the pulsar within the unpulsed extended nebula.

The extended emission has a total size of ∼50 mas with a position angle (P.A.) of approximately −75°. Visual inspection of higher-resolution images shows that the structure is dominated by a bright compact core and a diffuse component. We fitted two components to the interferometric *uv*-plane using the task UVFIT. We found that the core is well fitted by a point-like component, whereas the diffuse emission is described by a circular Gaussian component

with a FWHM of 20 mas located at -32.0 ± 0.2 and 8.7 ± 0.2 mas from the core in right ascension and declination, respectively. It was not possible to fit an additional component for the pulsar, which is too faint to be distinguished from the core component with the current noise level.

The position of the pulsar, obtained from the difference between the gated and the ungated data, is 3.1 ± 0.3 mas in right ascension and -4.6 ± 0.4 mas in declination from the core component as seen with the current resolution, for a total separation of 5.6 ± 0.4 mas. The position of the pulsar is marked with a cross in Fig. 2, and its size is the estimated uncertainty at 5-σ level. The uncertainty in the relative astrometry of the pulsar comes from the limitation of efficiently subtracting the nebula contribution in the two images (gated and ungated), mainly because of small differences in the self-calibration and the determination of the scaling factor for the amplitudes, which is 0.25. We explored a range of the scaling factors between 0.15 and 0.35 and considered only those images showing a point-like source, i.e. for which the nebula was completely subtracted. We measured the pulsar position in each image, which followed a linear displacement as a function of the scaling factor. The maximum separation of these peak positions was divided by two to estimate the position uncertainty. An independent estimate of the position uncertainty comes from the fitting procedure of the JMFIT task within AIPS. We have considered the higher of these two values in each coordinate as the estimate of the 1-σ uncertainty in position, which turns out to be 0.3 mas in right ascension and 0.4 mas in declination. The cross plotted in Fig. 2 represents five times these values to be on the conservative side, given possible differences related to the self-calibration processes.

3 INFRARED SPECTROSCOPY

We performed European Southern Observatory (ESO) Very Large Telescope (VLT) observations of PSR B1259-63 on Unit Telescope 1 (UT1-Antu), using the Target of Opportunity (ToO) programme ID 086.D-0511 (PI Chaty) dedicated to optical/infrared study of high energy transients in support to *Fermi* observations. We obtained low-resolution ($R =\sim 750$) infrared spectra with the Infrared Spectrometer And Array Camera (ISAAC) instrument in near-infrared (NIR, SWS-LR JHKs 1-2 microns) on January 22/23 and March 12, 2011. The ToO was activated in two dates spaced by ~ 1.5 month, in January and March 2011, to compare two different sets of data, and potentially detect spectral variability of the source. Because of the brightness of the NIR counterpart (Ks=7.248), and to avoid non-linearity, the exposure time of individual ISAAC SW spectra was set to 3.55 s. Observations were carried out under clear conditions with a seeing ranging from 0.35 to 0.50 arcsec. Spectra analysis was standard, including zero correction, flat field correction, extraction, and wavelength calibration, using standard slit spectroscopy routines in the Image Reduction and Analysis Facility (IRAF) suite [3].

We show in Figure 3 both NIR Ks band spectra obtained in January and March 2011, where we clearly see two strong lines in emission: HeI and Brγ. We show in Figure 4 a zoom on the region including the Brγ line, to see the evolution of its profile between

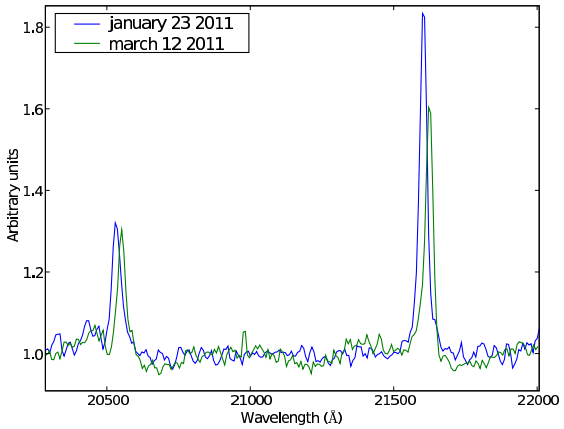

Figure 3. ESO/VLT NIR Ks band spectra obtained in January 23 and March 12, 2011.

the two observing dates. We also report in Table 1 the characteristics of HeI and Brγ lines: wavelength, equivalent width (EW) and Full Width Half Maximum (FWHM). We estimate the uncertainty of these parameters to $\sim$ 10% due to spectra analysis and localisation of the continuum by eye inspection (using the IRAF task *splot*). The overall uncertainty on wavelength calibration is due both to the instrumental resolution and to extraction of lamp spectrum, which are of the order of $\sim$ 0.3 nm and $\sim$ 2 nm respectively. Some lines appear at fit wavelength offset with respect to their laboratory position, with an offset greater in January than in March (see Table 1). While this offset might be created by Doppler effect of ejecta outflowing from the decretion disk, since we do not detect any similar offset at optical wavelengths, we can not exclude the possibility that this offset is due to larger uncertainty on wavelength calibration.

By comparing these NIR Ks-band spectra to the optical spectrum exhibiting a strong Hα line, and to the series of optical spectra centered on the HeI 6678 line, we observe the same general tendency both in optical and infrared, i.e. in both cases the EW of Hα and Brγ lines gradually decrease between January and March 2011 (compare Figure 1 panel e with Figure 4, and Table 2 with Table 1). In addition, the Brγ line is asymmetric (as the HeI 6678 line), with the blue wing slightly wider in March than in January, which is reminiscent of the asymetric double peaked HeI 6678 line. This asymmetry may indicate either the presence of a spiral density wave in the disk as suggested by the observations of HeI 6678 line, or even a truncation of the disk size between the compact object and the companion star (such as described in Okazaki & Negueruela (2001); Okazaki et al. (2011)). We note that the asymmetric wing could also be explained by the presence of ejecta outflowing from the decretion disk.

Finally, we notice that, while the intensity of the HeI line remains stable, the one of the Brγ line decreases between January and March observations, which might indicate a change in ionization in the part of the disk where these lines are created.

4 OPTICAL SPECTROSCOPY

Spectroscopic observations of LS 2883, the optical counterpart of PSR B1259−63, were performed with the CTIO 1.5m telescope,

[3] IRAF is distributed by the National Optical Astronomy Observatory, which is operated by the Association of Universities for Research in Astronomy (AURA) under cooperative agreement with the National Science Foundation. IRAF is available online at http://iraf.noao.edu/ .

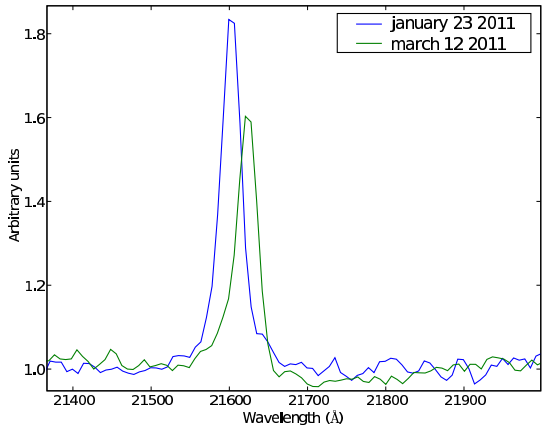

Figure 4. ESO/VLT NIR Ks band spectra obtained in January 23 and March 12, 2011, enlarged on the region including the Brγ line.

Table 1. Identified lines in ESO/VLT NIR Ks band spectra obtained in January 23 and March 12, 2011

Date	Line	λ_{lab}(Å)	λ_{fit}(Å)	EW (Å)	FWHM (Å)
January	HeI	20580	20531	-10.6	35.3
March	HeI	20580	20549	-10.1	32.2
January	Brγ	21661	21601	-25.2	30.3
March	Brγ	21661	21622	-20.4	32.0

operated by SMARTS consortium [4], between UT dates 2010 December 5 and 2011 May 17. We used the RC spectrograph in service observing mode with the standard SMARTS grating setup 47/Ib (grating 47 in 1st order) with the GG495 order sorting filter to achieve a wavelength coverage of 5630–6940 Å and a resolving power $R = \lambda/\Delta\lambda = 2500$ in the vicinity of the Hα line. We observed LS 2883 for 3×300 seconds each night for a total of 21 nights. Neon comparison lamp spectra were obtained before and after the sequence for wavelength calibration. The spectra were zero corrected, flat fielded, extracted, and wavelength calibrated using standard slit spectroscopy routines in IRAF. For each night of observations, we coadded the available spectra to improve the signal-to-noise (S/N) of weak lines, especially He I λ6678, before rectifying the mean spectrum to a unit continuum using line-free regions. The mean spectrum is shown in Fig. 5.

Over the 6 months of our observations, we detected changes in the overall strength of the Hα emission but no significant line profile variations. The equivalent width of the Hα line, $W_{\mathrm{H}\alpha}$, was measured by integrating over the emission line profile. We use the convention that an emission line has a negative $W_{\mathrm{H}\alpha}$, so the absolute value of $W_{\mathrm{H}\alpha}$ is shown in Fig. 1, panel (e). Although the He I λ6678 line has much lower S/N than Hα, we also measured its equivalent width, W_{6678}. The errors in $W_{\mathrm{H}\alpha}$ and W_{6678} are about 5% and 10%, respectively, due to noise and continuum placement. We compare W_{6678} (multiplied by 100 for better contrast) and $W_{\mathrm{H}\alpha}$ in panel (e) of Fig. 1. Although there is more scatter in the W_{6678} measurements, we found that the overall strength of He I λ6678 generally tracks the strength of Hα well. Table 2 lists the UT date, MJD, time relative

[4] http://www.astro.yale.edu/smarts

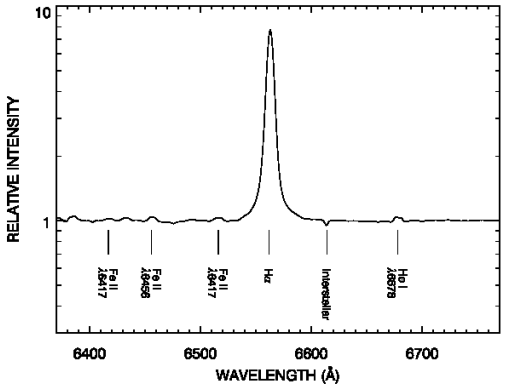

Figure 5. The mean Hα spectrum of LS 2883 is plotted with several other faint emission lines. The relative intensity is plotted on a log scale to emphasize the weaker emission lines.

to periastron passage, measured $W_{\mathrm{H}\alpha}$, and measured W_{6678} values for each observation in columns 1–5.

A growth of the equivalent width of the Hα line was observed from $-W_{\mathrm{H}\alpha} \simeq 62$ Å around 5 days before periastron until $-W_{\mathrm{H}\alpha} \simeq 75$ Å about 10 days after it. A decrease in $W_{\mathrm{H}\alpha}$ was observed later, although the poor sampling only allows us to constrain the start of the decrease between $t_{\mathrm{p}} + 18$ days and $t_{\mathrm{p}} + 46$ days, when it was back to $-W_{\mathrm{H}\alpha} = 62$ Å (note that a baseline level of $-W_{\mathrm{H}\alpha} = 54$ Å was measured at apastron by Negueruela et al. 2011). We interpret the observed behavior as the growth/decay of the mass and size of the Be star disk, caused by the interactions with the pulsar/pulsar wind. Unfortunately due to data sparsity we don't know the exact date when the behaviour of the line EW starts to decrease, but if future observations during following periastron passages confirm the possible coincidence of the decrease of $W_{\mathrm{H}\alpha}$ with the onset of the γ-ray flare, then it could point to a possible triggering mechanism of the flare: an abrupt change in the state of the circumstellar disk of the massive star. We explore this possibility in more detail in the Sect. 8.1.

Figure 6 shows the evolution of the He I λ6678 line profile. Despite the low resolving power of our observations, in most of our spectra the line is resolved with a clear double-peaked shape. The profile is symmetric within the limits of the S/N during the initial period up to $\sim t_{\mathrm{p}} + 20$ days. At later times, the line shows a clear excess in the blue side (negative velocities) of the line relative to the red.

5 X-RAY OBSERVATIONS AND RESULTS

We conducted an X-ray monitoring campaign on PSR B1259−63 with *XMM-Newton Swift* and *Suzaku* telescopes, covering the period between $t_{\mathrm{p}} - 131$ days and $t_{\mathrm{p}} + 79$ days. These observations are summarized in Tables 3, 4 and 5. Each of these tables lists an identifier for the data set, UT date, MJD, time relative to periastron passage, true anomaly of the orbit, and exposure time for each observation.

5.1 *XMM-Newton* observations

The log of the *XMM-Newton* data analyzed in this paper is presented in Table 3. In all *XMM-Newton* observations, the source

Table 2. Journal of 2010-2011 optical spectroscopic observations of PSR B1259−63 and properties of the Be circumstellar disk of LS 2883 (see Sect. 8.1 for details).

Date	MJD (days)	$t - t_p$ (days)	$W_{H\alpha}$ (Å)	W_{6678} (Å)	r ($R_\star$)	ρ_0 (10^{-11} g cm^{-3})	$R_{disk}/R_\star$	M_{disk} ($10^{-8} M_\odot$)
2010-12-05	55535.362	−9	−62.3	−0.44	33.6	2.82	8.8	1.31
2010-12-09	55539.341	−5	−62.0	−0.39	28.1	2.79	9.1	1.16
2010-12-12	55541.997	−3	−64.5	−0.39	25.7	3.03	9.5	1.19
2010-12-15	55545.304	1	−66.4	−0.46	24.9	3.20	9.7	1.24
2010-12-18	55548.312	4	−70.0	−0.52	26.4	3.56	10.0	1.43
2010-12-20	55549.997	5	−73.0	−0.48	28.1	3.86	10.2	1.61
2010-12-23	55553.305	9	−74.8	−0.55	32.5	4.05	10.1	1.85
2010-12-24	55554.342	10	−74.4	−0.52	34.0	4.00	10.0	1.88
2011-01-01	55562.319	18	−74.7	−0.56	47.4	4.04	9.3	2.31
2011-01-29	55590.226	46	−61.6	−0.40	91.2	0.60	7.7	0.50
2011-02-04	55596.000	52	−59.7	−0.45	99.2	0.58	7.5	0.51
2011-02-12	55604.290	60	−58.0	−0.43	110.0	0.44	7.4	0.39
2011-02-14	55606.307	62	−57.2	−0.42	112.6	0.44	7.3	0.38
2011-03-07	55627.231	83	−56.6	−0.35	137.3	0.43	7.3	0.38
2011-03-08	55628.002	83	−56.3	−0.37	138.2	0.43	7.3	0.38
2011-03-15	55635.002	90	−57.2	−0.43	145.7	0.44	7.3	0.38
2011-03-19	55639.002	94	−57.2	−0.42	149.9	0.44	7.3	0.38
2011-03-23	55643.163	98	−56.2	−0.42	154.2	0.43	7.2	0.38
2011-04-03	55654.003	109	−55.4	−0.42	164.9	0.42	7.2	0.37
2011-04-06	55657.003	112	−54.0	−0.38	167.8	0.42	7.1	0.37
2011-05-17	55698.004	153	−54.6	−0.31	203.3	0.42	7.1	0.37

Table 3. Journal of 2011 *XMM-Newton* observations of PSR B1259−63.

Data Set	Date	MJD (days)	$t - t_p$ (days)	ϕ (deg)	Exposure (ks)	f_{mos1}	f_{mos2}
X14	2011-01-06	55567.7	22	86.14	13.49	1.020 ± 0.007	0.967 ± 0.007
X15	2011-02-02	55594.8	49	112.26	13.58	1.05 ± 0.01	1.05 ± 0.01
X16	2011-03-04	55624.2	79	278.57	8.10	1.02 ± 0.02	1.05 ± 0.02

was observed with the European Photon Imaging Cameras (EPIC) MOS1, MOS2 (den Herder et al. 2001) and PN (Strüder et al. 2001) detectors in the small window mode with a medium filter. The *XMM-Newton* Observation Data Files (ODFs) were obtained from the online Science Archive[5] and analyzed with the Science Analysis Software (SAS) v11.0.0. During the data cleaning, all events that have energies above 10 keV and a count rate higher than 0.5 cts s^{-1} for the PN or 0.35 cts s^{-1} for the MOS detectors were removed.

The event lists for spectral analysis were extracted from a 22.5′′ radius circle for the MOS1 and MOS2 observations and from a 45′′ radius circle for the PN observations. For the spectral analysis, we made a simultaneous fit to the MOS1, MOS2 and PN data without imposing constraints on the intercalibration factors. The values of the MOS1 and MOS2 intercalibration factors f_{mos1}, f_{mos2} relative to the PN are given in the last two columns of Table 3.

5.2 *Swift* observations

Swift has closely monitored the PSR B1259−63 2010 periastron passage, and the data log is shown in Table 4. The Swift/X-ray Telescope (XRT) (Gehrels et al. 2004) data were taken in photon mode with 500 × 500 window size. We processed all the data with standard procedures using the FTOOLS[6] task `xrtpipeline` (version 0.12.6 under the HEAsoft package 6.12). We extracted source events from a circular region with a radius of 1′, and to account for the background we extracted events from a nearby circle of the same radius. Due to the low countrate (less than 0.4 cts s^{-1}), no pile up correction was necessary.

After spectral extraction, the data were rebinned with a minimum of 25 counts per energy bin to allow χ^2 fitting. The anciliary response file was generated with `xrtmkarf`, taking into account vignetting and point-spread function corrections. In our analysis we used the `swxpc0to12s6_20070901v011.rmf` spectral redistribution matrix for observations Sw5, Sw10, Sw11 and Sw12. For Sw6, Sw7, Sw8, Sw9 `swxpc0to12s6_20010101v013.rmf` was used instead.

The first set of *Swift* observations was taken in August 2010, when the source flux was rather weak. After checking that the spectrum of the source varies only within the error limits during these observations, we combined all the *Swift* August data in order to have better statistics (Sw5 observation).

[5] http://xmm.vilspa.esa.es/external/xmm_data_acc/xsa/index.shtml

[6] http://heasarc.gsfc.nasa.gov/docs/software

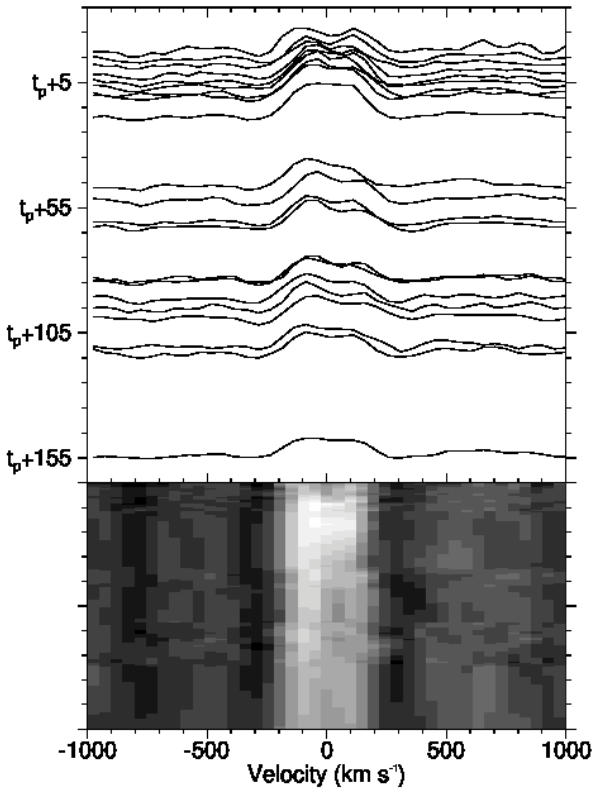

Figure 6. The upper plot shows the He I λ6678 line profile of LS 2883 over the 6 months of observation, sorted by MJD, and the lower plot shows a gray-scale image of the same line. The intensity at each velocity in the gray-scale image is assigned one of 16 gray levels based on its value between the minimum (dark) and maximum (bright) observed values. The intensity between observed spectra is calculated by a linear interpolation between the closest observed phases.

Table 4. Journal of 2010-2011 *Swift* observations of PSR B1259−63.

Data Set	Date	MJD (days)	$t - t_p$ (days)	ϕ (deg)	Exposure (ks)
Sw5	2010-08-06	55414.3	−131	210.6	2.98
	2010-08-08	55416.0	−129	210.8	3.29
	2010-08-09	55417.4	−128	211.1	3.34
	2010-08-12	55420.0	−125	211.5	2.41
	2010-08-15	55423.2	−122	212.0	3.19
Sw6	2010-11-20	55520.2	−25	255.2	3.87
Sw7	2010-11-25	55525.6	−19	264.5	4.18
Sw8	2010-11-30	55530.5	−14	276.5	3.36
Sw9	2010-12-14	55544.6	−1	355.6	4.30
Sw10	2011-01-19	55580.7	35	117.0	3.98
Sw11	2011-01-20	55581.0	36	117.2	4.17
Sw12	2011-01-22	55583.7	38	119.5	4.13

5.3 *Suzaku* observations

There were three *Suzaku* observations taken shortly after the 2010 periastron passage of PSR B1259−63 (see Table 5). The *Suzaku* observations were performed with three X-ray CCDs (the X-ray Imaging Spectrometers or XISs; Koyama et al. 2007) in the range 0.3–12 keV and the Hard X-ray Detector (HXD; Takahashi et al. 2007) in the range 13–600 keV. The XISs consists of one back-illuminated CCD camera (XIS-1) and two front-illuminated CCDs (XIS-0 and XIS-3). In this paper we discuss only the results of the XIS observations, while the HXD data will be discussed in a separate paper. Our analysis was performed using the HEAsoft software package (version 6.12).

Table 5. Journal of 2011 *Suzaku* observations of PSR B1259−63.

Data Set	Date	MJD (days)	$t - t_p$ (days)	ϕ (deg)	Exposure (ks)
Sz9	2011-01-05	55566.8	22	99.6	90.0
Sz10	2011-01-24	55585.6	41	121.0	40.3
Sz11	2011-02-02	55594.2	49	126.5	21.5

We analyzed the XIS data using pipeline processing version 2.5.16.29. We made use of cleaned event files of the XIS observations, with standard event screening applied. The standard screening procedures include event grade selections and the removal of time periods such as the spacecraft passage through the South Atlantic Anomaly, intervals of small geomagnetic cutoff rigidity, and times of low elevation angle. We found that XIS-0 gives somewhat lower $N_{\rm H}$ than others, which is most likely caused by imperfect calibrations due to the recently-changed behavior of contamination buildup. Thus we report the results from XIS-1 and XIS-3 only. A joint spectral fitting of XIS-1 and XIS-3 was done in the energy range of 0.4–9.5 keV.

5.4 The X-ray lightcurve

Panel (c) of Fig. 1 shows the X-ray lightcurve of the system. Observations made with different instruments at close orbital phases are consistent with each other, demonstrating good intercalibration.

From data obtained at orbital phases similar to the archival observations of previous periastron passages, one can see that the system orbital lightcurve is stable over several year timescales. The stability of the orbital lightcurve allows us to use old and new data simultaneously while analyzing the orbital evolution of the flux. The sharp rise of the X-ray flux at $t \sim t_p - 25$, probably related to the pulsar entering the Be star disk, in 2010 was closely followed by Swift (observations Sw6 - Sw8). During this time, the flux increased by a factor of 4 in nine days (note that due to the sparse observations, we probably missed the maximum flux). As the pulsar moved towards the periastron passage, the flux gradually decreased, reaching a local minimum that is only half the peak value near the periastron. Afterwards, we followed the system through its second passage near the disk, when we again observed an increase in flux to a value approximately 1.4 times higher than the maximum value observed during the first disk crossing. After that, the X-ray flux gradually decreased in a good agreement with previous observations, showing no unusual behavior during the time of the GeV flare.

5.5 Spectral Analysis

The X-ray spectral analyses were done with NASA/GSFC XSPEC v12.7.1 software package. A simple power law with a photoelectric absorption describes the data well, with no evidence for any line features. In Table 6 we present the results of the three parameter fits to the *XMM-Newton*, *Swift* and *Suzaku* data in the 0.5–10 keV energy range. The uncertainties are given at the 1σ statistical level

Table 6. Spectral parameters for 2010-2011 observations of PSR B1259−63.

Data Set	$t - t_p$ (days)	F(1–10 keV) (10^{-11} erg cm^{-2} s^{-1})	Γ	N_H (10^{22} cm^{-2})	χ^2(ndof)
Sw5	−127	$0.17^{+0.01}_{-0.02}$	1.8 ± 0.09	0.5	8.3 (14)
Sw6	−25	$0.69^{+0.08}_{-0.16}$	$0.99^{+0.13}_{-0.23}$	0.5	3.6 (7)
Sw7	−19	1.53 ± 0.12	1.33 ± 0.08	0.5	25.48 (24)
Sw8	−14	$2.60^{+0.12}_{-0.16}$	1.37 ± 0.06	0.5	61.73 (35)
Sw9	−1	$1.72^{+0.11}_{-0.08}$	1.56 ± 0.05	0.5	47.9 (39)
Sz9	22	3.56 ± 0.01	1.76 ± 0.01	0.56 ± 0.01	2177 (2454)
X14	22	$3.25^{+0.01}_{-0.02}$	1.71 ± 0.01	0.48 ± 0.04	2220 (2029)
Sw10	35	$2.31^{+0.08}_{-0.11}$	1.51 ± 0.06	0.5	36.1 (41)
Sw11	36	$2.19^{+0.09}_{-0.10}$	1.48 ± 0.06	0.5	44.7 (42)
Sw12	38	$2.02^{+0.12}_{-0.05}$	1.44 ± 0.06	0.5	33.2 (41)
Sz10	41	2.08 ± 0.02	1.53 ± 0.01	0.51 ± 0.01	1566 (1528)
X15	49	$1.61^{+0.02}_{-0.01}$	1.45 ± 0.01	0.44 ± 0.01	1418 (1453)
Sz11	49	$1.77^{+0.02}_{-0.04}$	1.46 ± 0.02	0.48 ± 0.01	749 (769)
X16	79	$1.13^{+0.02}_{-0.01}$	1.37 ± 0.02	0.42 ± 0.01	855(851)

and do not include systematic uncertainties. The quality of the *Swift* data does not allow us to look for both spectral slope and absorption column density, so we decided to fix the latter to the value $N_H = 5 \times 10^{21}$ cm^{-2} consistent with the value found in the *XMM-Newton* and *Suzaku* observations.

Similar to the observations of previous periastron passages, we found that several months before the periastron the spectral index was quite soft, $\Gamma \sim 1.8$. It became much harder a month before periastron, as the flux started to increase. The spectrum softened a bit as the flux reached its maximum, but it remained harder than $\Gamma = 1.5$. The spectrum softened again as the pulsar approached periastron and entered the disk for the second time. At the moment when the X-ray luminosity reached its second peak the slope was softer than $\Gamma = 1.7$. As the X-ray luminosity started to decrease the slope remained close to 1.5, except during the very last *XMM-Newton* observation, when the slope became hard again, reaching the value $\Gamma = 0.42$ previously observed at $t - t_p = +266$ days (Chernyakova et al. 2006).

6 *Fermi*-Ł OBSERVATIONS AND RESULTS

The *Fermi Gamma-ray Space Telescope* was launched on 2008 June 11, from Cape Canaveral, Florida. The Large Area Telescope (LAT) is an electron-positron pair production telescope, featuring solid state silicon trackers and cesium iodide calorimeters, sensitive to photons from ∼ 20 MeV to greater than 300 GeV (Atwood et al. 2009). Relative to earlier γ-ray missions, the LAT has a large ∼ 2.4 sr field of view, a large effective area (∼ 8000 cm^2 for > 1 GeV on axis) and improved angular resolution (PSF is better than 1° for 68% containment at 1 GeV). The *Fermi* survey mode operations began on 2008 August 4. In this mode, the observatory is rocked north and south on alternate orbits to provide more uniform coverage so that every part of the sky is observed for about 30 minutes every 3 hours.

The analysis of the *Fermi*-Ł data in this paper is similar to the method used in Abdo et al. (2011b). We used the P7SOURCE data set and the associated P7SOURCE_V6 instrument response functions. The analysis was performed using the *Fermi* Science Tools 09-27-01 package [7]. A zenith angle cut of < 100° was applied to the data to reject atmospheric γ-rays from the Earth's limb. The standard binned maximum likelihood analysis was performed on events extracted from a 20° × 20° region around the location of PSR B1259−63 in the energy range 0.1–300 GeV. The source model used in the maximum likelihood analysis included 2 years (2FGL) *Fermi* catalog (Nolan et al. 2012) γ-ray sources within the analysed region, PSR B1259−63 and the diffuse Galactic and extragalactic components. Galactic diffuse emission was modelled using the `gal_2yearp7v6_v0.fits` model, and the isotropic diffuse component was modelled using the `iso_p7v6source.txt` model. The Ł data analysed in this paper covers the 4.5 years period between 2008 August 4 and 2013 February 19. This covers the time period over which the pulsar was near apastron until well after the passage of the pulsar through the dense equatorial disk of the Be star.

First we analysed the whole 4.5 years of available data, modelling the spectrum of each point source with a catalog model. The normalizations and indexes of catalog point sources as well as the normalization of the extragalactic diffuse background were then fixed to their best-fit values in order to build the PSR B1259−63 lightcurve around the periastron. The power law index of PSR B1259−63 was fixed to the best-fit value (2.86) obtained for the time period around the periastron passage. Afterwards, the normalizations of PSR B1259−63, Galactic diffuse background and the sources marked as variable in 2FGL catalog (within 5° from PSR B1259−63) were left free, similar to the procedure used by Abdo et al. (2011b).

Panel (b) in Fig. 1 shows the Ł flux light curve. All data points have a significance higher than 2 σ. The upper limits on the figure corresponds to 95% confidence limit. The time binning was selected to be 7 days for the period of the flare and 14 days otherwise. The light curve shows upper limits until $t_p - 25$ days, detections around a flux level of 0.5×10^{-6} cm^{-2} s^{-1} between $t_p - 25$ days and $t_p + 16$ days, and the GeV flare that reaches a flux level of 2×10^{-6} cm^{-2} s^{-1} at $t_p + 30$ days and decays in a roughly linear way, with the last detection at a flux level of 0.5×10^{-6} cm^{-2} s^{-1} between $t_p + 65$ days and $t_p + 80$ days. The results obtained in this

[7] FSSC is available online at http://fermi.gsfc.nasa.gov/ssc/data/analysis/software/

paper are consistent with those in the earlier work by Abdo et al. (2011b).

7 H.E.S.S. OBSERVATIONS AND RESULTS

The High Energy Stereoscopic System (H.E.S.S.) is an array of imaging atmospheric Cherenkov telescopes located in the Khomas Highland of Namibia at an altitude of 1800 m above sea level. H.E.S.S. phase I (consisting of four 13 m diameter telescopes) is optimized for the detection of very high energy γ-rays in the range of 100 GeV to 20 TeV. The total field of view is 5° and the angular resolution of the system is $\lesssim 0.1°$. The average energy resolution is about 15%. The H.E.S.S. I array is capable of detecting point sources with a flux of 1% of the Crab nebula flux at a significance level of 5σ in 25 hours when observing at low zenith angles (Aharonian et al. 2006).

Observations of PSR B1259−63 around its 2010 periastron passage resulted in a rather small dataset compared to observations around the 2004 (Aharonian et al. 2005) and 2007 (Aharonian et al. 2009) periastron passages. The collected data correspond to a live-time of about 6 h (H.E.S.S. Collaboration et al. 2013). Observations were performed over five nights, 2011 January 9/10, 10/11, 13/14, 14/15 and 15/16, which corresponds to the period from $t_p + 26$ to $t_p + 32$ with respect to the time of periastron.

The source was detected at the 11.5 σ level (Li & Ma 1983) at a position compatible with previous H.E.S.S. observations. The differential spectrum of the source follows a simple power-law with a flux normalization at 1 TeV $N_0 = (1.95 \pm 0.32_{\rm stat} \pm 0.39_{\rm syst}) \times 10^{-12}$ TeV^{-1} cm^{-2} s^{-1} and spectral index $\Gamma = 2.92 \pm 0.30_{\rm stat} \pm 0.20_{\rm syst}$. The integral flux above 1 TeV averaged over the entire observation period is $F(E > 1\ \text{TeV}) = (1.01 \pm 0.18_{\rm stat} \pm 0.20_{\rm syst}) \times 10^{-12}$ cm^{-2} s^{-1} (H.E.S.S. Collaboration et al. 2013). The nightly lightcurve over the observation period (panel (a) in Fig. 1) is compatible with a constant flux and does not show any hint of source variability (H.E.S.S. Collaboration et al. 2013).

Both the flux level and spectral shape from 2011 are in a very good agreement with results obtained for previous periastron passages. Moreover, the comparison of results obtained in 2011 and 2004 observations, which were taken at similar orbital phases, provides a stronger evidence of the repetitive behavior of PSR B1259−63 (see Fig. 1) (H.E.S.S. Collaboration et al. 2013). Such comparison was not possible using the 2004 and 2007 data sets as observations were performed at different phases before and after periastron.

H.E.S.S. observations provide a three-day overlap ($t_p + 30$; $t_p + 32$) in time with the GeV flare detected by *Fermi*. This allows the direct study of a possible flux enhancement in the TeV band over the timescale of the GeV flare. A careful statistical study showed no evidence of any significant flux enhancement, which leads to the conclusion that the GeV flare emission is of a different nature than the TeV emission (H.E.S.S. Collaboration et al. 2013).

8 DISCUSSION

The broad-band non-thermal emission from the PSR B1259−63 system is produced in the interaction of the relativistic pulsar wind with the stellar wind of the massive Be star. The high eccentricity of the orbit is responsible for the episodic nature of the source activity, with bright outbursts occurring during the periods of the pulsar's close passage near the massive star. The characteristic "double peak" structure of the orbital lightcurves of the source in the radio, X-ray and, possibly, TeV γ-ray bands is naturally interpreted as occurring due to the inhomogeneity of the stellar outflow of the fast-rotating Be star. The peaks of the non-thermal emission are associated with the periods of the pulsar's passage through the denser and slower gas in the equatorial disk of the Be star. This behavior has also been observed during the previous periastron passages and is clearly seen in the radio and X-ray bands also during the 2010-2011 periastron passage, shown in Fig. 1.

The orbit-to-orbit lightcurves in the radio band, which are qualitatively similar with the maxima occurring at similar orbital phases, exhibit up to $\sim$ 50% differences in the overall flux level between different periastron passages (Johnston et al. 2005). Contrary to the radio lightcurve, the behavior of the source in the X-ray band is remarkably stable. Measurements of the X-ray flux at the same orbital phases, spaced by several 3.4 yr orbital periods, reveal nearly the same flux.

Fermi LAT observations of the 0.1–10 GeV γ-ray activity of the source during the 2010-2011 periastron passage have revealed a puzzling flaring activity, which occurred after the periastron passage and also after the post-periastron transit of the equatorial disk of the Be star by the pulsar. The GeV flaring activity was remarkable in the sense that the energy output of the source in this band reached a theoretical maximum given by the spin-down luminosity of the pulsar, 8×10^{35} erg s^{-1}, assuming isotropic emission in this energy band. Abdo et al. (2011b) have noticed that the GeV band flare was peculiar in the sense that it had no obvious counterparts at lower energies, in the radio and X-ray bands.

The broad-band observations of the source reported here generally support the conclusion of Abdo et al. (2011b) on the "orphan" nature of the GeV flare. The only data that could reveal an irregularity in the source behavior coincident in time with the moment of the GeV flare are the optical spectroscopic data shown in panel (e) of Fig. 1. These data show a clear decrease of the equivalent width of the Hα line that could coincide with the GeV flare. A gap in the optical spectroscopy data during the period 18–46 days after the periastron does not allow us to tell if the decrease of $W_{\rm H\alpha}$ is exactly coincident with the moment of the GeV flare (30 days after the periastron). However, it seems that the decrease of the line strength is delayed with respect to the start of the radio outburst that happened 15 days after the periastron. The peculiar behavior of the Hα line and its possible relation to the GeV flare deserve special attention.

8.1 Evolution of the Be star disk mass and size based on the Hα line measurements

With multiple observations of $W_{\rm H\alpha}$ available, we can estimate the changing size and mass of the circumstellar disk through the periastron passage. Grundstrom & Gies (2006) describe a simple model to measure the ratio of the projected effective disk radius (the radius at which half of the Hα emission originates) to the stellar radius, $R_{\rm disk}/R_\star$, and the density at the base of the disk, ρ_0, using $W_{\rm H\alpha}$, the stellar effective temperature $T_{\rm eff}$, and disk inclination angle $i_{\rm disk}$ as input parameters.

Negueruela et al. (2011) found that LS 2883 is highly distorted due to its rapid rotation, with a polar radius (or equivalent non-rotating radius) $R_\star = 8.1\ R_\odot$ and a bulging equatorial radius $R_{\star,\rm eq} = 9.7\ R_\odot$. The equator is significantly cooler than the poles (27500 K vs. 34000 K) due to gravity darkening. They also found that the Be star is inclined with 33° and has an angular velocity Ω of about 88% of the critical rotation value at which the cen-

trifugal force at the equator equals the gravitational force. Using a Roche model for such a rapidly rotating star (Maeder 2009), we find that the mean temperature averaged over the stellar surface is about 30200 K, so we define $T_{\rm eff}$ accordingly.

For LS 2883, the Be disk should be highly truncated near periastron, both due to the gravitational influence of the pulsar (which is observed in other Be binaries using long baseline optical interferometry; Gies et al. 2007) and due to disruption by the pulsar wind ram pressure (predicted by simulations of Okazaki et al. 2011; Takata et al. 2012). The truncation distance expands rapidly after periastron passage. Therefore we used the orbital solution of Wang, Johnston & Manchester (2004), a stellar mass of 31 $M_\odot$ (Negueruela et al. 2011), and the typical neutron star mass of 1.4 $M_\odot$ to calculate the binary separation distance, r, as a function of time. The separation values range from 24.8 $R_\star < r < 203.3$ $R_\star$ over the course of our observations. We fixed the outer disk boundary to r when the stars are close ($r < 100$ $R_\star$), and we used an outer boundary of 100 $R_\star$ in accordance with the recommendation of Grundstrom & Gies (2006) for times when $r > 100$ $R_\star$.

To estimate the total mass of the disk, we used an axisymmetric, isothermal density distribution,

$$\rho(r,z) = \rho_0 \left(\frac{R_\star}{r}\right)^n \exp\left[-\frac{1}{2}\left(\frac{z}{H(r)}\right)^2\right] \quad (1)$$

(Carciofi & Bjorkman 2006) and a radial density exponent $n = 3$, typical of other Be star disks (Gies et al. 2007). The scale height of the disk is

$$H(r) = H_0 \left(\frac{r}{R_\star}\right)^\beta, \quad (2)$$

where

$$H_0 = \frac{a}{V_{\rm crit}} R_\star, \quad (3)$$

$$a = \sqrt{\frac{kT}{\mu m_{\rm H}}}, \quad (4)$$

and $\beta = 1.5$ for an isothermal disk (Bjorkman & Carciofi 2005; Carciofi & Bjorkman 2006). We integrated this density distribution from the equatorial stellar surface at $R_{\star,\rm eq}$ out to the disk truncation radius, described above, to estimate the total disk mass, $M_{\rm disk}$.

The resulting ρ_0, $R_{\rm disk}/R_\star$, and $M_{\rm disk}$ are listed in Table 2. We emphasize that these disk measurements should be viewed with caution since our assumption of an axisymmetric, isothermal disk is overly simplistic. Deviations from this simple disk structure may produce order of magnitude variations in the calculated mass, and these effects are discussed more throughly by McSwain et al. (2008). A further source in error for our disk mass measurement is the truncation radius assumed in our model. For a pulsar orbit that is inclined 90 degrees relative to the Be disk, the separation distance when the pulsar becomes eclipsed by the disk, 42.2 $R_\star$, is slightly higher than the periastron distance. This implies slightly higher disk masses near periastron. However, if the disk is truncated instead at the star's effective Roche lobe radius, then we predict slightly lower disk masses. These revised masses are well within the order of magnitude error that is inherent to the assumptions of our model.

Within our model we found that the Be disk grew in mass as the binary went through periastron passage in 2010 December. Tidal disruption by the neutron star may have triggered this sudden growth in disk mass. Moreno, Koenigsberger & Harrington (2011) find that the rate of energy dissipation over the stellar surface reaches a maximum amplitude near or slightly after periastron passage in very eccentric binaries, prompting an increase in stellar activity near that orbital phase. Other Be stars (eg. δ Sco; Miroshnichenko et al. 2001, 2003) have been observed to exhibit disk outbursts around the time of periastron passage, so the disk growth of LS 2883 is not unusual.

The times of GeV flaring in PSR B1259−63 correspond to an epoch of disk reduction. We speculate that the GeV flaring could be due to the interaction of a mass stream being pulled away from the disk to collide with the relativistic pulsar's wind.

Additional information on the properties of the disrupted disk could be found from the He I λ6678 line profile, shown in Fig. 6. Despite the low resolving power of our observations, in most of our spectra the line is resolved with a clear double-peaked shape. During the disk growth period, the peaks are symmetric within the limits of the S/N. However, during the disk reduction period, the He I λ6678 line shows a clear excess in the blue side of the line (negative velocities) relative to the red one. The asymmetry is sustained for at least ~ 60 days, far longer than the expected 1–2 days required for disk material to circle the star. The asymmetry may indicate a slowly moving spiral density wave in the disk, typical of density waves observed in other Be stars (Porter & Rivinius 2003). The pulsar wind probably does not significantly alter the ionization levels in the circumstellar disk. Since He I will ionize at a lower temperature than H I, it would be expected to be fully ionized near periastron if the pulsar wind's influence on the disk produces strong ionization effects. However, we observe that the Hα and He I λ6678 line strengths track each other well in Fig. 1, and no significant deviations are found within the limits of noise. The similarities with other Be stars in binary systems, which suffer gravitational disruption, and the non alteration of the disk ionization, suggest that the disk disruption seen in the optical data might simply be driven by gravitational tidal forces instead of a pulsar interaction.

8.2 The radio outflow during the GeV flare

The high-energy particle outflow from the system is unresolved in most of the energy bands except for the radio. Both previously reported high-resolution observations in the radio band (Moldón et al. 2011) and the observations reported here reveal the extended nature of the radio source, about 50 mas in size. At a distance $d \simeq 2$ kpc (Negueruela et al. 2011), this corresponds to a projected linear size of the source $R \simeq 1.5 \times 10^{15}\,[d/2\,{\rm kpc}]$ cm, which is two orders of magnitude larger than the orbital separation at periastron. Our analysis of the high-resolution LBA image obtained 29 days after the 2010 periastron passage has two important implications.

Firstly, we have found a radio structure that is very similar to the one found 21 days after the 2007 periastron passage (see Fig. 1-middle in Moldón et al. 2011). This confirms the presence of an extended structure in each periastron passage and their similar appearances, albeit with a slightly more negative position angle in the image presented here. This may be a consequence of the different orbital phases of the observations, and it will be discussed in a future paper including four additional LBA observations conducted around the 2010 periastron passage.

Secondly, the position of the pulsar is determined for the first time with the same data used to obtain the radio morphology of the nebula extending towards the North-West, allowing us to make a direct measurement of the pulsar's position inside the nebula. We found that the pulsar is located around 5 mas towards South-East

of the peak of the radio nebula. This is still marginally compatible with the predicted pulsar position in the 2007 periastron passage (see the red cross in Fig. 1-middle in Moldón et al. 2011), which was an indirect estimation affected by unmodelled ionospheric uncertainties that also depended on the uncertain proper motion of the binary system and on the orbital motion of the pulsar around the massive star. With the relative positions of the pulsar and the nebula obtained here, we find that the overall morphology of the source is consistent with a cometary tail extending behind the pulsar.

The projected displacement of the peak of the nebular emission from the pulsar position, $R_{\rm r} \simeq 1.5 \times 10^{14}\,[d/2\ {\rm kpc}]$ cm, provides an estimate of the distance scale at which the optical depth becomes comparable to the free-free absorption, which suppresses the radio emission from the innermost region. The measured distance to the radio emitting region is in a good agreement with the estimate of Zdziarski, Neronov & Chernyakova (2010)

$$R_{\rm r} \simeq 2\times 10^{14}\left[\frac{\dot{M}_{\rm w}}{10^{-7}\ M_\odot\ {\rm yr}^{-1}}\right]^{2/3}\left[\frac{v_\infty}{10^8\ {\rm cm\ s}^{-1}}\right]^{-2/3}\times \qquad (5)$$
$$\times\left[\frac{\nu}{2.3\ {\rm GHz}}\right]^{-2/3}\left[\frac{T}{3\times 10^4\ {\rm K}}\right]^{-1/2}\left[\frac{f}{0.1}\right]^{-1/3}\ {\rm cm}$$

for a typical mass loss rate of the Be star $\dot{M}_{\rm w}$, asymptotic speed, v_∞, clumping factor, f, and temperature, T, of the stellar wind. For PSR B1259−63 the terminal velocity of the wind was estimated to be 1350 ± 200 km s^{-1} (McCollum 1993).

The radio emission is produced via the synchrotron mechanism by electrons with energies (Zdziarski, Neronov & Chernyakova 2010)

$$E_{\rm e,r} \simeq 0.1\left[\frac{B_{\rm r}}{10\ {\rm mG}}\right]^{-1/2}\left[\frac{\nu}{1\ {\rm GHz}}\right]^{1/2}\ {\rm GeV} \qquad (6)$$

where $B_{\rm r}$ is the strength of magnetic field in the radio emission region. If such electrons are (a) injected during the GeV flare and (b) are able to escape towards the radio emission region with the speed comparable to the speed of light, they would reach the radio emission region in less than two hours from the start of the flare. Therefore, the absence of a radio counterpart of the GeV flare (mostly from archival data at similar orbital phases) implies that either the 100 MeV electrons are not injected during the flare or they escape at a speed much lower than the speed of light.

Slow escape of the radio-emitting plasma has been recently revealed in the observations of another γ-ray loud binary system, LS I +61 303 (Chernyakova et al. 2012), in which the speed of the high-energy particle loaded outflow was found to be comparable to the speed of the stellar wind. Adopting such a model for the PSR B1259−63 system would imply a time delay $t_{\rm r} = R_{\rm r}/v_\infty \simeq$ 17 days for the radio "echo" of the GeV flare. This time period was not covered by the ATCA radio observations reported here (see panel (d) of Fig. 1), so it remains unclear whether the GeV flare was associated with a delayed radio counterpart or whether electrons with energies in the ~ 0.1 GeV range were injected in the flare. No evidence of such a flare is present in the archival data (see panel (d) of Fig. 1 for the details of 2004 periastron passage), but at the moment we do not know whether the GeV flare occurs each periastron passage so we cannot make any firm conclusions.

8.3 X-ray and TeV observations

Similarly to the radio observations, neither X-ray nor the TeV observations reveal obvious counterparts to the GeV flare. However, contrary to the radio emission, the X-ray and TeV emission are, most probably, produced directly inside the binary orbit so that no time delay of the X-ray and TeV band emission is expected.

Although the time coverage of the HESS TeV lightcurve during the 2010-2011 periastron passage is not sufficient to draw definitive conclusions on the presence/absence of the TeV flaring activity during the whole period of the GeV band flare, a careful statistical study showed no evidence of any significant flux enhancement in TeV energy band right at the beginning of the GeV flare (H.E.S.S. Collaboration et al. 2013). Moreover, one could notice from the top panel of Fig. 1 that the TeV flux measurements one month after the periastron are consistent with the previous measurements during the 2004 periastron passage at similar times. This indicates that the orbit-to-orbit behavior of the source in the TeV band might be stable, similar to the behavior in the X-ray band. In fact, the X-ray and TeV band flux might be produced by one and the same electron population with ∼TeV energies, via the synchrotron and inverse Compton mechanisms. If this is the case, one could combine the 2004 and 2010-2011 data into an orbit-folded lightcurve. Such a lightcurve would reveal a broad post-periastron maximum compatible with the post-periastron maxima of the X-ray and radio lightcurves, but there is no pronounced maximum occurring at the moment of the GeV band flare (see Fig. 1).

In the X-ray band, non-simultaneous data from different periastron passages are compatible with the interpretation that the post-periastron maximum of the lightcurve may have a two-peak structure (see Fig. 1). Based on the observed trend in the post-periastron X-ray lightcurve, we should expect the X-ray flux about 30 d after the periastron to decline. However, instead we see that the 2007 *Chandra* flux at t_p + 29 days is comparable to the the 2010 measurements by *Suzaku* and *XMM-Newton* some 22 days after the periastron. Thus, the flux observed by *Chandra* in 2007 at $t_p + 29$ days might be an X-ray counterpart to a GeV flare (if the GeV flare is a periodic phenomenon). However, similarly to the case of the TeV observations, it is not possible to draw definitive conclusions on the presence/absence of the X-ray counterpart of the GeV flare because of the lack of the systematic monitoring of the source close to the flare period.

Repeated observations of the source during the next periastron passage, with a denser time coverage both in X-rays and in the TeV band, are essential to clarify the existence of the X-ray and TeV counterparts of the GeV flare as well as the question of the recurrent nature of the flare.

8.4 Possible connection of the Be star disk perturbation and the GeV Flare.

In this paper we discuss the possibility that the detected GeV flare could be related to the reduction in the size/mass of the equatorial disk of the massive Be star in the system. Unfortunately, a gap in the Hα data does not allow us to make a firm identification of the start of the GeV flare with the start of the decrease of the equivalent width of the Hα line. The possibility of triggering the flare by the disk disruption event has to be verified with the future observations with denser coverage of the Hα measurements around the onset of the flare.

The decrease of $W_{\rm H\alpha}$ and the enhanced blue wing of the He I λ6678 line indicate the presence of strong perturbations in the interacting pulsar wind - stellar wind system. In the absence of perturbation of the Be star disk, the relativistic particles can escape from the system along a bow-shaped contact surface of the pulsar and stellar winds and in a direction opposite to the contact surface

apex. A part of the pulsar wind power emitted not in the direction of the bow shock apex is able to escape to large distances, like in a typical large-scale pulsar wind nebula. Only the power emitted in the direction of the bow shock is converted to radiation.

In the model discussed in Kong, Cheng & Huang (2012) the observed X-ray and GeV emission is explained as synchrotron emission from the postshock relativistic electrons Doppler-boosted at the particular orbital phase. This model is able to describe the observed spectra pretty well, but fails to explain the substantial shift of the X-ray and GeV light curve peaks.

In the modelling one should take into account that the strong perturbation of the disk destroys the regular bow-shaped contact surface between the pulsar and stellar outflow. It is possible that the fly-by of the disk material near the pulsar destroys the regular geometry of the relativistic particle and electromagnetic field flow in the unshocked pulsar wind. Once the magnetic field in the pulsar wind ceases to be aligned with the particle flow, high-energy particles in the wind immediately lose their energy via synchrotron radiation. In such a scenario the energy of electrons responsible for the GeV flare should be in the 100 TeV range:

$$E_{\rm e,flare} \simeq 10^2 \left[\frac{B_{\rm pw}}{1\ {\rm G}}\right]^{-1/2} \left[\frac{\nu}{1\ {\rm GHz}}\right]^{1/2}\ {\rm TeV} \qquad (7)$$

assuming that magnetic field in the pulsar wind is at the level of $B_{\rm pw} \sim 1$ G at distances comparable to the binary separation distance ($\sim 10^{13}$ cm). The energy of electrons responsible for the highest energy synchrotron emission is in the 100 TeV range, which is close to the PeV energies of electrons responsible for the recently discovered GeV flares of the Crab pulsar / pulsar wind nebula system (Abdo et al. 2011a; Buehler et al. 2012). This suggests a possibility that, in both sources, the flares could be produced via the same mechanism. In the case of the Crab flares, the short timescale $t_{\rm crab} < 1$ day of the variability suggests a relatively compact size of the flaring source of $l_{\rm crab} \leqslant 10^2$ AU. This distance scale is comparable to the size of the extended source revealed by the VLBI observations of PSR B1259−63. Taking this into account, the appearance of 100 TeV electrons responsible for the γ-ray synchrotron emission in the PSR B1259−63 system does not appear unreasonable.

In the synchrotron scenario, the duration of the flare is estimated by the time of the fly-by of the disk material near the pulsar, so that 10–30 days is a reasonable estimate, assuming a typical speed of the stellar wind and taking the binary separation distance as the estimate of the size of the region occupied by the pulsar wind.

The absence of the flare counterparts in the radio, X-ray and TeV bands could also be reasonably explained by the high efficiency of synchrotron energy losses for the 100 TeV particles. Most of the power of the pulsar wind is converted into the GeV band emission, with only minor fraction of the power left for emission at much lower energies. Synchrotron cooling of the 100 TeV particles would form a characteristic $dN/dE \sim E^{-2}$ low-energy tail in the electron distribution. The spectrum of synchrotron emission from this low-energy tail would have a slope $dN_\gamma/dE \sim E^{-1.5}$, so that the power emitted in the X-ray band is some ~ 3 orders of magnitude lower than the power of the GeV band emission. Taking into account that the luminosity of inverse Compton emission in the TeV band is comparable to the luminosity of the X-ray emission, one arrives at a conclusion that no TeV band counterpart of the flare is expected to be detectable.

An alternative possibility is that the GeV flaring emission is produced via the inverse Compton, rather than synchrotron, mechanism. Such a possibility was considered by Khangulyan et al. (2012). In this case, the energies of electrons in the unshocked pulsar wind are much lower, in the GeV range. A fraction of the observed GeV emission from the system is thus produced via inverse Compton scattering of the UV radiation coming either directly from the Be star or from its circumstellar disk by the unshocked pulsar wind electrons. The fraction of the GeV flux produced in this way depends on the geometry of the region occupied by the unshocked pulsar wind. The luminosity of the inverse Compton emission from the unshocked pulsar wind could strongly increase if the volume occupied by the unshocked pulsar wind increases. This scenario requires a very high efficiency of reprocessing stellar radiation in the Be star disk, with up to a half of the UV luminosity of the system being due to the emission from the disk, rather than from the star.

A strong perturbation of the equatorial disk of the Be star could, in principle, lead to an enhancement of the luminosity of the inverse Compton emission from the unshocked pulsar wind. Indeed, a natural consequence of the destruction of the disk is that the volume occupied by the unshocked pulsar wind rapidly grows. Electrons/positrons in the unshocked pulsar wind propagate to larger distances and could give away a larger fraction of their energy to the inverse Compton radiation while remaining in the unshocked wind. With a suitable assumption about the UV luminosity of the circumstellar disk (which turns out to be very high, exceeding the stellar luminosity, possibly as a result of local heating of the Be star disk by the pulsar crossing, see Khangulyan et al. (2012)), one could find that nearly 100% of the spin-down luminosity of the pulsar could be converted into γ-ray power in the unshocked wind if its volume becomes sufficiently large during the flare.

A potential problem of such a scenario would be to explain why the inverse Compton luminosity of the system does not reach the spin-down luminosity of the pulsar before the destruction of the disk. Indeed, before the disk destruction, the volume occupied by the unshocked pulsar wind is small so that the efficiency of the inverse Compton energy loss in the unshocked pulsar wind zone is low. As a result, the inverse Compton luminosity of the unshocked wind is much less than 100% of the spin-down power. However, electrons and positrons from the pulsar wind do not stop to lose energy via the inverse Compton emission when they enter the shocked pulsar wind zone at the same rate as in the unshocked pulsar wind zone. If the unshocked pulsar wind electrons/positrons release 100% of their energy into the inverse Compton emission while escaping from the system during the flaring period, the shocked pulsar wind electrons/positrons should also release 100% of their energy via the same channel while escaping through the shocked pulsar wind before the flare. Thus, the inverse Compton luminosity of the system is expected to be at 100% of the pulsar spin-down power throughout the pulsar's passage through the disk, not only at the moment of the disk destruction. A possible way out of this difficulty might be the existence of an alternative non-radiative channel of energy dissipation of the pulsar wind electrons/positrons in the shocked pulsar wind region, a question that requires further investigation.

Besides the optical photons coming from the star and the disk, X-ray photons produced by the shocked pulsar wind can act as seed photons for the observed GeV emission. Such a possibility was discussed by Pétri & Dubus (2011) and Dubus & Cerutti (2013). In Pétri & Dubus (2011) GeV emission is generated rather close to the pulsar, and the X-ray photons are scattered by the relativisitic pairs in the striped pulsar wind. In this case the GeV flare was interpreted by the authors as a lucky combination of the geometry and a presence of additional seed photons coming from the shocked region. In the Dubus & Cerutti (2013) model the GeV emission is due to the IC scattering of the X-ray photons by the schocked relativistic

wind. In this model the GeV flare is expected to peak near the inferior conjunction, but the reason of the delay between the X-ray and GeV peak in this model is not clear.

Mochol & Kirk (2013) interprete the observed flare as IC scattering of the optical photons on the precursor of superluminal waves roughly 30 days after the periastron passage. This model does not require an additional source of photons, but it is unclear what triggers the formation of the precursor well after the exit from the disk. This model also predicts a preperiastron flare, which has not been observed at any wavelength.

9 CONCLUSIONS

In this paper, we have reported the results of multi-wavelength observations of PSR B1259−63 during its 2010 periastron passage. This was the first periastron for which complete monitoring in the high-energy gamma-ray band was available. These data have revealed a puzzling GeV flare occurring $\simeq$ 30 days after the periastron (Abdo et al. 2011b). Our multi-wavelength data show that the source behavior in the radio and X-ray band is qualitatively similar to the previous periastron passages and that there are no obvious counterparts of the GeV flare in other wavebands, from radio to TeV γ-rays. However, both in the X-rays and radio data from previous periastron passages there might be small irregularities in the behaviour of the lightcurves at the moment of the onset of the GeV flare. The possible relation of these irregularities to the GeV flare has to be verified with simultaneous data during future multi-wavelength campaign for the next periastron passage.

The orbital lightcurves in the radio band do exhibit orbit-to-orbit variations. On the other hand, the X-ray lightcurve is remarkably stable. This might be related to the fact that the X-ray emission is produced directly inside the binary system, while the radio emission is produced by the high-energy outflow reaching distances 10–100 times larger than the binary system size. The time coverage of the source in the TeV band is not sufficient to judge whether the source is variable from orbit to orbit.

Optical spectroscopy data reveal the evolution of the Hα line strength, which indicates changes in the state of the circumstellar disk of the Be star induced by the close passage of the pulsar. The pulsar first induces growth of the disk in mass and size. The disk growth stops after the periastron passage and further interaction of the pulsar / pulsar wind with the disk leads to a perturbation of the disk structure, which possibly triggers the GeV band flare. This perturbation manifests itself in the reduction of the equivalent widths of the Hα and He I λ6678 lines. On the other hand, the disk disruption that we observe may be a normal occurrence in binary Be systems due to gravitational interactions near the close passage. Unfortunately, the optical spectroscopy data have a gap at the moment of the onset of the GeV flare, so we are not able to make an unambiguous link between the flare onset and changes in the Be star disk state. This possible link should be verified with a denser optical spectroscopy coverage of the periastron passage in 2014.

We have measured for the first time the position of the pulsar and the unpulsed extended emission from the same data set in the radio band. Such a measurement removes the systematic uncertainty related to the cross-calibration of different data sets which has affected previous measurements. This measurement pinpoints the position of the binary system within an extended radio emission region of the size $\sim$ 100 AU. We find that the overall morphology of the radio source is compatible with a "cometary tail" extending behind the pulsar.

There are a number of open questions that should be addressed in new multi-wavelength observations during the next periastron passage in 2014. In particular, it is not clear whether the GeV flare is recurrent and, if it is, whether it occurs at a particular orbital phase. The triggering mechanism of the flare has to be clarified. We should investigate more deeply possible multi-wavelength signatures of the triggering mechanism of the flare with new simultaneous observations densely covering the time span of the flare. Our results point to a possible relationship between the GeV flare and changes in the Be star disk state. These changes could hopefully be traced by the variations of the strength of emission lines from the disk or of its column density.

10 ACKNOWLEDGEMENTS

The *Fermi* LAT Collaboration acknowledges support from a number of agencies and institutes for both development and the operation of the LAT as well as scientific data analysis. These include NASA and DOE in the United States, CEA/Irfu and IN2P3/CNRS in France, ASI and INFN in Italy, MEXT, KEK, and JAXA in Japan, and the K. A. Wallenberg Foundation, the Swedish Research Council and the National Space Board in Sweden. Additional support from INAF in Italy and CNES in France for science analysis during the operations phase is also gratefully acknowledged.

The Parkes radio telescope and the Australian Long Baseline Array are part of the Australia Telescope which is funded by the Commonwealth Government for operation as a National Facility managed by CSIRO. We thank our colleagues for their assistance with the radio timing observations. This work made use of the Swinburne University of Technology software correlator, developed as part of the Australian Major National Research Facilities Programme and operated under licence.

A.N. is grateful to the Swiss National Science Foundation for the support under grant PP00P2_123426/1. M. V. M. is grateful for support from the National Science Foundation under grant AST-1109247 and from NASA under DPR number NNX11AO41G. J.M., M.R. and J.M.P. acknowledge support by the Spanish Ministerio de Economía y Competitividad (MINECO) under grants AYA2010-21782-C03-01 and FPA2010-22056-C06-02. J.M. acknowledges support by MINECO under grant BES-2008-004564. M.R. acknowledges financial support from MINECO and European Social Funds through a *Ramón y Cajal* fellowship. J.M.P. acknowledges financial support from ICREA Academia.

Based on observations made with ESO Telescopes at the La Silla Paranal Observatory under programme ID 086.D-0511. This work was supported by the Centre National d'Etudes Spatiales (CNES), based on observations obtained with MINE -the Multi-wavelength INTEGRAL NEtwork.

The authors thank the International Space Science Institute (ISSI, Bern) for support within the ISSI team "Study of Gamma-ray Loud Binary Systems" and SFI/HEA Irish Centre for High-End Computing (ICHEC) for the provision of computational facilities and support.

REFERENCES

Abdo A. A. et al., 2011a, Science, 331, 739
Abdo A. A. et al., 2011b, ApJ, 736, L11
Aharonian F. et al., 2009, A&A, 507, 389

Aharonian F., Akhperjanian A. G., Aye K., Bazer-Bachi, et al., 2005, A&A, 442, 1
Aharonian F. et al., 2006, A&A, 457, 899
Atwood W. B. et al., 2009, ApJ, 697, 1071
Bjorkman J. E., Carciofi A. C., 2005, in Astronomical Society of the Pacific Conference Series, Vol. 337, The Nature and Evolution of Disks Around Hot Stars, Ignace R., Gayley K. G., eds., p. 75
Buehler R. et al., 2012, ApJ, 749, 26
Carciofi A. C., Bjorkman J. E., 2006, ApJ, 639, 1081
Chernyakova M., Neronov A., Aharonian F., Uchiyama Y., Takahashi T., 2009, MNRAS, 397, 2123
Chernyakova M., Neronov A., Lutovinov A., Rodriguez J., Johnston S., 2006, MNRAS, 367, 1201
Chernyakova M., Neronov A., Molkov S., Malyshev D., Lutovinov A., Pooley G., 2012, ApJ, 747, L29
den Herder J. W. et al., 2001, A&A, 365, L7
Dubus G., Cerutti B., 2013, A&A, 557, A127
Gehrels N. et al., 2004, ApJ, 611, 1005
Gies D. R. et al., 2007, ApJ, 654, 527
Grundstrom E. D., Gies D. R., 2006, ApJ, 651, L53
H.E.S.S. Collaboration et al., 2013, A&A, 551, A94
Hirayama M., Cominsky L. R., Kaspi V. M., Nagase F., Tavani M., Kawai N., Grove J. E., 1999, ApJ, 521, 718
Johnston S., Ball L., Wang N., Manchester R. N., 2005, MNRAS, 358, 1069
Johnston S., Manchester R. N., Lyne A. G., Bailes M., Kaspi V. M., Qiao G., D'Amico N., 1992, ApJ, 387, L37
Johnston S., Manchester R. N., Lyne A. G., D'Amico N., Bailes M., Gaensler B. M., Nicastro L., 1996, MNRAS, 279, 1026
Johnston S., Manchester R. N., McConnell D., Campbell-Wilson D., 1999, MNRAS, 302, 277
Khangulyan D., Aharonian F. A., Bogovalov S. V., Ribó M., 2012, ApJ, 752, L17
Kirk J. G., Ball L., Skjaeraasen O., 1999, Astroparticle Physics, 10, 31
Kong S. W., Cheng K. S., Huang Y. F., 2012, ApJ, 753, 127
Koyama K. et al., 2007, PASJ, 59, 23
Li T.-P., Ma Y.-Q., 1983, ApJ, 272, 317
Maeder A., 2009, Physics, Formation and Evolution of Rotating Stars, Astronomy and Astrophysics Library. ISBN 978-3-540-76948-4. Springer Berlin Heidelberg, 2009
McCollum B., 1993, in Bulletin of the American Astronomical Society, Vol. 25, American Astronomical Society Meeting Abstracts, p. 1321
McSwain M. V., Huang W., Gies D. R., Grundstrom E. D., Townsend R. H. D., 2008, ApJ, 672, 590
Melatos A., Johnston S., Melrose D. B., 1995, MNRAS, 275, 381
Miroshnichenko A. S. et al., 2003, A&A, 408, 305
Miroshnichenko A. S. et al., 2001, A&A, 377, 485
Mochol I., Kirk J. G., 2013, ApJ, 776, 40
Moldón J., Johnston S., Ribó M., Paredes J. M., Deller A. T., 2011, ApJ, 732, L10
Moldón J., Ribó M., Paredes J. M., 2012, A&A, 548, A103
Moreno E., Koenigsberger G., Harrington D. M., 2011, A&A, 528, A48
Negueruela I., Ribó M., Herrero A., Lorenzo J., Khangulyan D., Aharonian F. A., 2011, ApJ, 732, L11
Nolan P. L. et al., 2012, VizieR Online Data Catalog, 219, 90031
Okazaki A. T., Nagataki S., Naito T., Kawachi A., Hayasaki K., Owocki S. P., Takata J., 2011, PASJ, 63, 893
Okazaki A. T., Negueruela I., 2001, A&A, 377, 161
Pavlov G. G., Chang C., Kargaltsev O., 2011, ApJ, 730, 2
Pétri J., Dubus G., 2011, MNRAS, 417, 532
Porter J. M., Rivinius T., 2003, PASP, 115, 1153
Smith D. A. et al., 2008, A&A, 492, 923
Strüder L. et al., 2001, A&A, 365, L18
Takahashi T. et al., 2007, PASJ, 59, 35
Takata J. et al., 2012, ApJ, 750, 70
Tam P. H. T., Huang R. H. H., Takata J., Hui C. Y., Kong A. K. H., Cheng K. S., 2011, ApJ, 736, L10
Tavani M. et al., 1996, A&AS, 120, C221+
Wang N., Johnston S., Manchester R. N., 2004, MNRAS, 351, 599
Weltevrede P. et al., 2010, PASA, 27, 64
Zdziarski A. A., Neronov A., Chernyakova M., 2010, MNRAS, 403, 1873